

Tropical South America/Atlantic sector convective margins and their relationship to low-level inflow

BENJAMIN R. LINTNER AND J. DAVID NEELIN

Department of Atmospheric Sciences, and Institute of Geophysics and Planetary Physics, University of California, Los Angeles

June 17, 2009

Abstract

Tropical convective margins are hypothesized to be sensitive to low-level inflow conditions. The present study evaluates where and to what extent convective margin variability is sensitive to low-level inflow variability using observed precipitation and reanalysis wind and total precipitable water data over the tropical South America/Atlantic sector in austral summer. Composite analysis based on an inflow measure defined by projecting low-level monthly-mean atmospheric boundary layer (ABL) or lower free troposphere (LFT) winds onto either mean horizontal precipitation or precipitable water gradients shows widespread contraction of the edges of convection zones in the direction of stronger convection for anomalously strong low-level inflow: such behavior is consistent with enhanced import of relatively dry air along the edges of convection zones. However, the distinction between ABL and LFT winds may be significant regionally, for example, along the Atlantic ITCZ northern margin. Back trajectory analysis is employed to estimate source regions of low-level air masses arriving at margin points over timescales (2-4 days) during which low-level air masses are expected to retain some memory of initial moisture conditions while also undergoing diabatic modification. Probability distribution functions of mean precipitation values encountered along trajectories facilitate objective quantification of the frequency with which trajectories approach the margin from drier areas outside the convection zone. While margin points in the ABL are strongly dominated by inflow (i.e., trajectories originating outside of the convection zone), points in the LFT may show inflow, outflow, or mixed inflow/outflow conditions. LFT locations dominated by inflow trajectories generally correspond to regions with composites exhibiting the clearest signatures of LFT wind variability on precipitation.

1. Introduction

Interactions between inflow air mass characteristics, particularly moisture, and convection are critical to understanding the observed multiscale organization and variability of tropical precipitation. Observational data from field campaigns identify important effects from synoptic intrusions of dry air on the climatology and variability of tropical precipitation (Numaguti et al., 1995; Yoneyama and Parsons 1999; Parsons et al., 2000; Sobel et al., 2004). High-resolution cloud resolving models demonstrate the impacts of lower free tropospheric moisture on simulations of convection and cloud statistics (Tompkins 2001; Redelsperger et al., 2002; Derbyshire et al., 2004). Process studies of various large-scale tropical phenomena, including El Niño/Southern Oscillation tropical teleconnections (Neelin et al., 2003), monsoons subject to modern or past boundary conditions (Chou and Neelin 2001; Su and Neelin 2005), and the South Pacific Convergence Zone climatology and synoptic scale variability (Takahashi and Battisti 2007; Lintner and Neelin 2008), point to the substantial role of moisture advection, particularly dry air originating outside of the convecting region (ventilation), in determining the precipitation characteristics of these phenomena.

In this study, we address the relationship between low-level inflow wind and tropical precipitation, especially in the spatial transitions between climatologically strongly-convecting and nonconvecting regions. These transition regimes, or convective margins, exhibit considerable variability across a range of timescales, with many tropical land margins particularly susceptible to severe droughts. Furthermore, global warming projections indicate that some of the most substantial impacts of anthropogenic climate change are likely to occur along convective margins; although the detailed spatial patterns differ considerably among current generation models, the ensemble of models suggests a tendency for reduced rainfall along tropical convective margins (Soden and Held 2006; Neelin et al., 2006; IPCC 2007).

In examining the inflow-related variability in precipitation along tropical convective margins,

we draw on insights from a simple analytic prototype developed for understanding the behavior of convective margins under conditions of mean low-level inflow from a dry region into the convection zone (Lintner and Neelin 2007, 2008, see Section 3 for details). Briefly, the convective margins prototype illustrates the dynamic and thermodynamic factors, i.e., low-level inflow windspeed, top-of the atmosphere radiative heating, inflow moisture, and a moisture threshold condition at which deep convection occurs, that set where the convective margin occurs. While quantitative application of the prototype is feasible under some circumstances, e.g., where the inflow into the convection zone is relatively steady, it may not be under more general conditions. Nevertheless, some qualitative utility is expected for anticipating how a convection zone responds to perturbations, and it is of interest to assess the degree to which the convective margins prototype is applicable in more realistic settings.

A straightforward means of quantifying the relationship between inflow air mass and precipitation is to composite precipitation variability onto a measure of low-level inflow, based here on the component of horizontal winds projected in the direction of mean precipitation or moisture gradients. This inflow diagnostic yields a straightforward measure of observed convective margin “shifts” in response to low-level inflow fluctuations. Since it is anticipated that the details of the vertical structure of low-level winds may affect inflow-convection sensitivity, we consider results based on both 1000 mb, atmospheric boundary layer (ABL), and 850 mb, or lower free troposphere (LFT), winds. Although we find widespread geographic agreement for composites based on the two pressure levels, there are locally large differences.

To complement the composite analysis, we present a survey of 5-day back trajectories terminating at points along the convective margin. The principal objective here is to identify and characterize the ABL and LFT source regions of air masses to the margin. The back trajectories also provide an indication of how representative the monthly Eulerian wind field is of the synoptic conditions that are directly responsible for moisture transport. For example, there is some correspondence between the relatively complex trajectory characteristics along the northern margin of

the Atlantic ITCZ and the locally weak LFT inflow-precipitation relationship seen there.

This study focuses on the tropical South America/Atlantic sector (90°W - 20°E , 40°S - 20°N) during the austral summer season (i.e., January-February-March, hereafter JFM). Much research has been devoted to understanding the climate variability of this region, especially over the continent, in large part because of the substantial droughts frequently experienced there (Hastenrath and Greischar 1993; Nobre and Shukla 1996; Zeng et al., 2008). For example, on interannual timescales, anomalously dry conditions over Nordeste Brazil frequently occur with El Niño conditions in the Pacific or anomalous meridional SST gradients in the Atlantic (Giannini et al., 2001). South American rainfall has also been shown to be influenced regionally by low-level wind regimes, e.g., anomalous easterlies and/or southerlies favor below-normal precipitation (e.g., Chaves and Cavalcanti 2001; Moscati and Gan 2007). Of course, even though specific regional and seasonal foci are adopted, we expect that insights regarding relationships of convective margin variability to low-level inflow gained here should apply in other regions and seasons, as we intend to explore in future work.

2. Data

The precipitation data analyzed here are the Climate Prediction Center (CPC) Merged Analysis of Precipitation (CMAP; Xie and Arkin 1997). The CMAP data consist of monthly mean merged satellite and rain gauge observations on a $2.5^{\circ} \times 2.5^{\circ}$ horizontal grid. The horizontal wind data are from the NCEP/NCAR Reanalysis (Kalnay et al., 1996). We consider winds at $2.5^{\circ} \times 2.5^{\circ}$ resolution on two pressure levels, one in the boundary layer (1000 mb) and one in the lower free troposphere (850 mb). Total precipitable water, also from the NCEP/NCAR Reanalysis, is used as proxy for column integrated moisture. The period of analysis spans 1979-2006.

3. Convective margins prototype perspective on low-level inflow variability

JFM climatologies of precipitation (shaded contours; in mm day^{-1}) and 1000 mb winds (arrows; in m s^{-1}) appear in Figure 1a. Additionally, a proxy delineating the convective margin, the mean CMAP 4 mm day^{-1} contour, is included (line contour). While the choice of margin proxy is arbitrary, the 4 mm day^{-1} contour is found to be frequently colocated with where both the simulated and reanalysis mean mid-tropospheric vertical velocity and vertically-integrated mean vertical moisture transport fields change sign (Chou et al., 2009). The orientation of the 1000 mb wind vectors indicates low-level inflow into much of the strongly-convecting region over the Atlantic Intertropical Convergence Zone (ITCZ), the Amazon Basin, and the South Atlantic Convergence Zone (SACZ).

We now examine precipitation variability along a mean low-level inflow trajectory. For simplicity, we consider a longitudinal transect along 10°S , since the JFM-mean 1000 mb flow is seen to be almost purely zonal at this location. Compositing on values of u_{1000} averaged over $45^\circ\text{--}35^\circ\text{W}$ demonstrates the effect of anomalous inflow on the CMAP precipitation profile (Figure 1b). In particular, weak easterlies (blue curve) are characterized by higher values of precipitation along the eastern edge of the continental convection zone.

a. Convective margins prototype configuration and assumptions

The vertically-integrated moisture (q) equation, in steady-state and with x denoting the distance along an inflow trajectory, may be approximated as

$$u_q \frac{dq}{dx} = E - P + M_q \omega \quad (1)$$

where u_q is the wind projected onto an *a priori* prescribed vertical structure of q (see Neelin and Zeng 2000, for further details); E is evaporation; P is precipitation, taken as $P = \epsilon_c(q - q_c)$ for $q > q_c$, with ϵ_c inversely proportional to a timescale for convective adjustment, τ_c ; $M_q = M_{qp}q$ is the moisture stratification; and ω is related to the windfield divergence. ω can be eliminated from

(1) by invoking the steady state, vertically-averaged tropospheric temperature T equation:

$$M_s \omega = F_T + P \quad (2)$$

where M_s is the dry static stability and $F_T = F_{NET} - E$, where F_{NET} is the sum of top-of-the-atmosphere radiative fluxes and surface radiative and turbulent fluxes. It is also useful to consider the moist static energy (MSE) equation, which can be obtained by adding (1) and (2), which eliminates P (in the absence of feedbacks onto F_{NET}):

$$M \omega = F_{NET} - u_q \frac{dq}{dx} \quad (3)$$

with $M = M_s - M_q$. Where q -gradients are small, (3) yields ω proportional to the net energy input into the atmospheric column.

b. Step function forcing

For the purpose of directly comparing the prototype solution to the 10°S transect in Figure 1b, values of the forcing parameters have been chosen to be representative of JFM-mean conditions in the tropical South America/Atlantic sector (Figure 2a). In particular, F_{NET} is modeled as a two-sided step function which is positive over land and negative over the ocean; the sign change can be understood by noting that over land, the steady state net surface flux is zero while top-of-the-atmosphere radiative heating is positive, and over ocean, dynamical oceanic heat flux divergence maintains nonzero (and in the present tropical case, negative) net surface heat flux. A spatially constant inflow wind is imposed producing both inflow and outflow margins.

Over the inflow oceanic area (Region I in Figure 2a), the form of the moisture solution is $q(x) = (q_0 - q_e)e^{-\lambda(x-x_0)} + q_e$. Here, $q_e = -E/(M_{qp}\omega)$ is the value of q determined by the balance of evaporation and (large-scale) moisture divergence. The length-scale $\lambda^{-1} = u_q M_s [M_{qp}(E - F_{NET})]^{-1}$ determines the spatial rate at which $q(x)$ asymptotes to q_e . For a zonal inflow path through the tropical Atlantic descent region, a typical q_0 may in fact be less than q_e because

southerly dry air advection (i.e., advection across the inflow path) offsets moistening by E . For simplicity, we set $q_0 = q_e$ so that $q(x) = q_e$. Thus, at the inflow land-ocean interface, the moisture value is q_e regardless of windspeed.

Because $q_e < q_c$ some portion of the continent (Region II) will be nonconvecting for $u_q > 0$. The strong spatial rate of change in $q(x)$ in Region II is generated by the increase in F_{NET} , and the decrease in E , both of which reduce divergence. With $E < F_{NET}$ the flow would in fact become convergent, although the evaporative effect on convergence is weaker than the direct effect of moistening by E (Lintner and Neelin 2009). After $q(x)$ reaches q_c (Region III), convection switches on and the rate of q -increase decreases. The length-scale $\lambda_c^{-1} \approx u_q \tau_c M_s M^{-1}$ determines the rate of convergence of $q(x)$ toward its asymptotic limit, $-(2a)^{-1}[b - (b^2 - 4ac)^{0.5}]$, where $a = M_{qp} M_s^{-1} \epsilon_c$, $b = M_{qp} M_s^{-1} (F_T - \epsilon_c q_c) - \epsilon_c$ and $c = E + \epsilon_c q_c$.

Referring again to the regional JFM climatologies of precipitation and 1000 mb winds in Figure 1a, it is also worth noting that some regions have a substantial component of the low-level circulation directed along, or even locally out of, the convection zone. A main motivation of the simple set-up here is comparison of the inflow and outflow margins. The asymmetry in Figure 2a arises from reduced sensitivity of outflow margin precipitation to low-level wind differences, as the precipitation in Region IV decays quickly after F_{NET} changes sign. At the outflow margin, λ_c^{-1} is the relevant length-scale, as the peak moisture value (which is close to the asymptotic limit for the wide $F_{NET} > 0$ region shown) on this margin decays toward q_c . In fact, in the limit of $\tau_c = 0$, the precipitation curves would decay to zero at the land-ocean interface F_{NET} . The reduced slope of the moisture curves after P becomes zero (Region V) is determined by λ^{-1} as the moisture relaxes toward q_e from above.

For the parameters shown in the idealized configuration, varying windspeed does not significantly alter the maximum P in the interior of the convection zone, although Figure 1b clearly reflects a non-negligible amplitude change. The maximum P in the idealized configuration would be impacted by changes to continental F_{NET} or the width of the forcing region (see next sub-

section). Also, observed wind speed changes occur in concert with changes to other quantities, such as vertically-integrated tropospheric temperature T . (T perturbations can directly alter peak precipitation values through the T -dependence of q_c .) Moreover, effects not incorporated into the simplest prototype, such as feedbacks between convection and low-level circulation, likely contribute.

c. Smoothed forcing

The prototype solution for a smoothly-varying but relatively narrow region of $F_{NET} > 0$ is shown in Figure 2b. The set-up depicted can be thought of as a simplistic representation of a portion of the ITCZ where the low-level flow crosses from one-side to the other. It also has analogy to simple models of Walker-like circulations and precipitation fronts (Bretherton and Sobel 2002; Frierson et al., 2004). Changing the windspeed is observed to affect the inflow margin of the convecting region. Moreover, in this case, the amplitude of the peak precipitation is reduced as the strength of the low-level wind increases. The decrease occurs as the width of the region above $q_c(T)$ with conditions favoring convergence feedback, i.e., $F_{NET} > 0$, decreases, owing to the shift (here to the right) of the location at which $q_c(T)$ is achieved on the inflow side. Again, the simple set-up here illustrates the asymmetry between the inflow and outflow margins, with the latter less sensitive than the former.

4. Precipitation variability associated with low-level inflow

a. Overview of precipitation variability

To provide a regional perspective of the CMAP precipitation variability, a pointwise difference map estimated from compositing on high and low precipitation values, i.e., values greater than 1σ or less than -1σ , at each gridpoint is shown in Figure 3. Here, composite differences (shaded contours) have been normalized by the JFM CMAP climatology at each gridpoint, with a cut-off

imposed for mean P values below 1 mm day^{-1} to avoid spurious effects of dividing by small values. Locations of the 4 mm day^{-1} contours for positive and negative phases are also indicated (green and brown lines, respectively), as are composite differences of 1000 mb winds.

Although the absolute precipitation variability increases as mean precipitation increases (not shown), normalization by the JFM precipitation climatology in Figure 3 emphasizes where the *relative* variability is largest, i.e., for low mean P . The locations of the 4 mm day^{-1} contours provide an indication of the geographic variability of the strongly convecting region. Notably, over the southwest tropical Atlantic/southeast tropical South America, the spatial separation of positive and negative phase contours is of roughly 20 degrees in longitude. Of course, since these contours are estimated from pointwise variations, they should be interpreted as providing estimates of the spatial domains over which strong convection is likely to occur rather than as realizations of the distribution of convection that would be observed for forcing conditions in different years.

b. Isolating the effect of low-level inflow variability

The typical orientation of the (u_{1000}, v_{1000}) composite difference vectors in Figure 3, directed from the negative phase 4 mm day^{-1} contour to the positive phase contour, indicates stronger precipitation occurs when at least some component of the anomalous low-level flow is directed out of the mean convecting region. We now demonstrate the influence of the low level inflow variability on precipitation. To do so, we define the monthly-mean precipitation gradient, $\vec{\nabla}P = (\partial_x P, \partial_y P)$ at each gridpoint, and then project u and v along it. The resulting scalar, $v_{\vec{\nabla}P}$, is signed negative (positive) for inflow (outflow) regions. For comparison, we also define $v_{\vec{\nabla}pw}$, the wind field projected onto the total precipitable water gradient, $\vec{\nabla}pw$, which should resemble $\vec{\nabla}P$ but is likely smoother.

JFM-mean composite differences for CMAP precipitation field conditionally-averaged on anomalies of $v_{\vec{\nabla}P}$ show, that over much of the Tropical South America/Atlantic sector, the point-

wise anomalous outflow minus inflow differences are positive (Figure 4a). Such behavior can again be qualitatively interpreted in the context of the LN07 prototype: for other parameters fixed (like the vertical moisture convergence or evaporation), pointwise strengthening of the low-level inflow increases the local analogue of λ^{-1} . The coincidence of the largest differences with (or below) the 4 mm day^{-1} contour is consistent with the presence of strong moisture gradients near the margins. The characteristic displacements of the 4 mm day^{-1} contour are of order $2.5\text{-}5^\circ$.

Dividing the composite differences in Figure 4b by the nonnormalized differences in Figure 3 yields a simple measure of the contribution of precipitation variability associated with low-level inflow to total precipitation variability at each gridpoint (Figure 5). Locally, up to 80 - 90% of the precipitation variability may be associated with fluctuations in 1000 mb inflow. An important caveat is that the association between inflow and precipitation as revealed by the compositing does not imply causality, especially given the use of monthly-mean fields. That is, it is possible that the low-level winds are responding to changes in convection generated through other mechanisms.

c. Sensitivity to lower tropospheric wind vertical structure

Compositing on the projection of the LFT (850 mb) wind field onto either the P or pw gradients yields broadly similar results to the ABL (Figure 6). However, despite the general agreement, there are some differences between the ABL and LFT composites. For example, rainfall along the northern Atlantic ITCZ margin appears relatively insensitive to anomalous inflow at the 850 mb level. On the other hand, precipitation over the interior of South America appears to vary more strongly with the winds in the LFT.

Comparison of the JFM climatologies of the horizontal wind fields at 1000 mb and 850 mb provides some insights into the composite characteristics seen at the two levels (Figure 7). Over the northern portion of South America, where the precipitation field is more sensitive to the 850 mb inflow variability, the JFM-mean winds in the lower free troposphere are much stronger than at the surface. Along the northern Atlantic ITCZ, the 850 mb flow tends to be effectively aligned with

the axis of the ITCZ, i.e., not strongly inflowing. Furthermore, while correlation of the monthly-mean inflow-projected ABL and LFT wind components suggests statistically strong coupling at the two levels over most of the tropical South America/Atlantic sector in JFM, the eastern tropical Atlantic in this season is notable for its lack of vertical inflow variability coherence through the lower troposphere.

d. Other sources of variability

We posit that the composite relationships between mean inflow changes and precipitation are consistent with the interpretation suggested by the convective margins prototype, namely the anomalous advection of mean moisture gradients ($-\bar{\mathbf{v}}' \cdot \vec{\nabla} \bar{q}$) yields $P' > 0$ for weaker inflow. Of course, mean advection of anomalous gradients ($-\bar{\mathbf{v}} \cdot \vec{\nabla} q'$) may also be significant, particularly since the shift of margin, which tends to be located where horizontal moisture gradients are large, may be associated with large q' . Where q' and $\bar{\mathbf{v}}'$ are both large, the second-order anomalous advection term ($-\bar{\mathbf{v}}' \cdot \vec{\nabla} q'$) may become non-negligible. As previously noted, covariation of low-level winds with other margin control factors (e.g., $q_c(T)$), may further contribute to the precipitation variability, though such effects are likely to be localized and suppressed by composite averaging.

Furthermore, pointwise compositing of precipitation on the gradient-normal (or along-contour) component of the low-level wind reveals non-negligible precipitation changes, especially along the eastern flank of the SACZ and over the subtropical and higher latitudes of South America (not shown). A prominent feature is the anomalous cyclone around the tip of the SACZ, with increased (decreased) precipitation to the north/east (south/west) resulting in an overall northeastward displacement of the SACZ axis. The features of this composite are reminiscent of the stationary eddy described by Robertson and Mechoso (2000). Their vorticity budget analysis demonstrates an equivalent barotropic structure and Rossby wave characteristics, with sizable contributions to the vertical motion field from vortex stretching and advection, which complicate relationships be-

tween circulation and convection. Moreover, the along-gradient and gradient-normal components of the low-level flow are not generally independent, e.g., some of the inflow variability into lower latitudes over eastern South America is connected to the anomalous low-level cyclonic circulation pattern centered to the south. Quantification of the relative influences of vorticity-related mechanisms and low-level advective moisture effects emphasized here is beyond the scope of the present study.

Additionally, some studies have found positive relationships between near-surface windspeed and oceanic precipitation rate (e.g., Raymond et al., 2003; Sobel et al., 2004), with the former assumed to be a proxy for latent heat flux. For the region and season considered here, however, pointwise compositing on windspeed (not shown) shows the opposite relationship is rather widespread, i.e., stronger low-level windspeeds are associated with reduced (oceanic) precipitation. At many locations, stronger windspeeds occur with enhanced low-level inflow into the convection zone. In fact, Sobel et al., (2004) suggest that the weakness of their inferred windspeed-precipitation relationship at Kwajalein in the western Pacific compared to that of the Raymond et al., (2003) analysis of the eastern Pacific ITCZ may reflect the trade-off between enhanced dry air advection and latent heat flux with increased surface winds. More strongly convecting oceanic regions, such as over the western Pacific warm pool, may behave differently from Atlantic ocean convection in that enhanced windspeeds might favor stronger evaporation in the absence of strong dry air advection from outside of the convection zone.

5. Characterizing convective inflow air mass source regions

In this section, we briefly examine the source regions of inflow into the convective margin. In particular, we use a trajectory model, the NOAA Air Resources Laboratory (ARL) Hybrid Single-Particle Lagrangian Integrated Trajectory (HYSPLIT; Drexler and Hess 1998), to estimate back trajectories of air masses reaching selected points along the convective margin.

a. HYSPLIT overview

HYSPLIT has been widely used to simulate long-range tracer transport, parcel dispersion, and pollution deposition. For the single particle trajectories considered here, HYSPLIT employs a predictor-corrector advection algorithm with a velocity-dependent timestep. The input meteorology data (here taken from $4 \times$ Daily NCEP/NCAR Reanalysis) are linearly interpolated in the horizontal from their $2.5^\circ \times 2.5^\circ$ native resolution and interpolated to a terrain-following sigma coordinate in the vertical. Although different vertical velocity formulations are possible, here the reanalysis-derived omega field is used. Back trajectories are initialized at noon local time for each day in March at selected convective margin target points at altitudes of 0.5 and 2.0 km.

In using the HYSPLIT back trajectories, we do not assume a strictly Lagrangian interpretation. Rather we expect that lower tropospheric air masses are modified by diabatic processes, including evaporation and shallow convection. A typical time scale to modify a cloudy boundary layer depends on the coefficient of the surface fluxes versus the depth of the layer, for instance, $H/(C_D v_s)$, where H is the layer depth, C_D is a drag coefficient, and V_s is the surface windspeed. For typical values, $H \sim 2\text{-}3$ km, $C_D \sim 0.001$, and $v_s \sim 7 \text{ ms}^{-1}$, this timescale is of order 3-5 days. We thus follow the trajectories for five days, considering the air mass properties to be determined by appropriately weighted averages along the trajectories.

The properties set in the non-precipitating descent region thus tend to be carried into the region where conditions become favorable to convection over a distance that depends on how quickly diabatic processes alter the air mass properties towards the onset of convection (i.e., a moisture value analogous to $q_c(T)$ in the simple prototype). The trajectories facilitate determination of the region where the air mass properties tend to be set as they are carried towards the convection zone. In future work, we plan to combine trajectory information with understanding of the moist diabatic and mixing processes acting to change moisture along trajectories to provide a trajectory-based view of convective margins and their variability, especially at higher frequencies where the

details of the time-evolution along trajectories is more critical.

b. Survey of March source regions and back trajectory characteristics

5-day back trajectories are displayed in Figures 8 (0.5 km) and 9 (2.0 km); for visual clarity, only 5 years of trajectories (2001-2005) are shown. The 0.5 km trajectories, which are primarily in the ABL, effectively show inflow at all locations displayed. For the target points on the northern margin of the Atlantic ITCZ, the trajectories originate in the trade wind flow of the North Atlantic; to the south of the ITCZ, the very low-level trajectories originate in the dry descent zone of the south tropical and subtropical Atlantic. Comparison of the 5 years illustrated suggests relatively constant source regions for most of the target points, although some systematic interannual differences are apparent. For example, the 2005 trajectories (purple) for the target points at 40°W, 11.25°S and 33.75°S, 7.5°S tend to be shorter than for the other years shown. The trajectories along the northern Atlantic ITCZ margin, as well as along the SACZ at 35°W, 20°S, are characterized by slightly larger day-to-day variability, underscoring more significant contributions of synoptic scale, midlatitude-originating weather systems to these trajectories.

Relative to the very low-level target points, the 2.0 km points—which typically lie above the ABL—manifest greater spatial dispersion. The more chaotic appearance of these trajectories reflects increased high-frequency variance of the higher altitude flow to these target points. While some systematic interannual differences are present, e.g., the 2002 trajectories terminating at 3°W, 2.5°S are typically longer than for the other years shown, these are largely masked by the greater synoptic variability. Nevertheless, the distributions of trajectories are sufficiently coherent to allow identification of typical source regions of inflow to points along the convective margin.

Unlike the 0.5 km trajectories, those for 2.0 km are not as pervasively dominated by inflow conditions. To illustrate this, we have computed probability distribution functions (pdfs) of the CMAP rainfall conditions encountered at 48, 72, and 96 hour intervals along the 2.0 km back trajectories (Figure 10). The 48 hour interval is chosen in the interest of isolating mean air mass

properties before they experience significant modification through potential feedbacks with local convective activity in the neighborhood of the target point. The 96 hour interval, by contrast, represents a plausible interval for which air mass properties in this portion of the troposphere may be expected to retain sufficient memory of “initial” conditions.

For most of the pdfs, the upstream flow typically originates in regions of lower mean precipitation (bins to the left of the target point precipitation shown by the dashed lines); that is, these target points reflect inflow conditions. (The highest percentage of inflow conditions at 72 hours is around 90%.) On the other hand, for the two points at 3°W , 2.5°S and 6.25°E , 6.25°S , the pdfs are weighted to the right side of the mean precipitation at the target point: these points are dominated by upstream outflow conditions, with trajectories over 48-96 hours tending to originate in regions of more intense convection (specially, over equatorial Africa—see Figure 9). The behavior of the pdf for the northern ITCZ margin target point in the middle of the Atlantic ITCZ is interesting in that it suggests outflow conditions at 48 and inflow conditions at 96 hours. Indeed, as suggested by Figure 9, these trajectories originate to the northeast of the target point before entering the mean convection zone.

c. Trajectory relationships to precipitation variability

We briefly consider how the characteristics HYSPLIT trajectories relate to precipitation variations by compositing the former on the interannual variations in March precipitation at 40°W , 11.25°S (Figure 11). For 5-day March back trajectories arriving at 2.0 km, there is an indication that low precipitation years are characterized by a longer 5-day trajectory path (red solid line). Additionally, there is a meridional separation of approximately 3° between the positive and negative phase trajectories. In the presence of a north-south SST gradient, the positive phase trajectories are likely somewhat moister.

It is also of interest to consider the evolution of *forward* trajectories initialized from a point within the inflow footprint. The point selected (30°W , 10°S , 1.6 km) lies near the median altitude

of back trajectories approximately 2 days upstream of 40°W , 11.25°S . For the results discussed here, variations in the initialization point made little qualitative difference.

The principal spatial features of the forward trajectory-precipitation composites include the penetration of the negative phase trajectory (red dashed line) into the South America to a day 5 position well past the target point. By contrast, the positive phase trajectory (blue dashed line) is seen to curve strongly to the south before reaching the target point: by day 5, the positive precipitation mean trajectory is located well to the south of its starting location in the main climatological axis of the SACZ.

The greater length of the negative-precipitation trajectory (i.e., measured in terms of the longitudinal displacement relative to the initialization point) is consistent with the back trajectory behavior as well as the Eulerian interpretation of the effect of stronger mean low-level inflow at this location. Faster low-level flow—here, enhanced easterly to southeasterly winds—means that for a given rate of diabatic air mass modification acting to increase moisture along the trajectory, e.g., vertical moisture convergence or ocean surface evaporation, the distance traveled before the initialized air mass reaches a specified moisture level is increased. For a fixed moisture threshold condition, this implies a westward shift of the convective margin.

On the other hand, the relative angular displacement of the trajectory phases implies additional processes than suggested by interpretation only in terms of strengthened mean inflow. To see this, it is instructive to consider the distribution of mean March winds shown in Figure 7 in the vicinity of the trajectories: in particular, the 850 mb winds are seen to be more northeasterly compared to the 1000 mb winds. The relative shift between the trajectories initialized at 1.0 (solid) and 0.5 (dashed) km is consistent with the angular displacement between the mean winds on the two levels. Moreover, examination of the composited vertical coordinates of the trajectories (not shown) suggests that the positive phase trajectories tend to experience more convergent conditions earlier along the trajectory relative to the negative phase trajectories. The more pronounced vertical displacement would lead to earlier influence by the more northeasterly flow at high levels, thereby

resulting in the greater curvature evident in the positive phase case.

6. Summary and conclusions

In this study, we consider the relationship between low-level inflow and the variability along the margins of tropical convection zones in the tropical South America/Atlantic sector using observed and reanalysis data. Using a definition of inflow into the convection zone comprising the low-level NCEP reanalysis wind field projected onto the horizontal gradient field of CMAP precipitation (or NCEP precipitable water), we demonstrated the relationship of stronger inflow into the convection zone and decreases in precipitation, particularly along the convective margins. Inflow-related precipitation variations may account for up to 80-90% of the precipitation variability in margin regions. The wind-precipitation relationship is consistent with the import of low-level air into the convection zone that tends to be dry relative to what is needed to convect. Conditioning the precipitation onto the inflow diagnostic defined using either atmospheric boundary layer or lower free troposphere winds yields broadly similar results, although the distinction between ABL and LFT may be important locally given vertical differences in the flow climatology and its variability.

Examination of 5-day back trajectories from the NOAA HYSPLIT model identifies the geographic source regions of low-level inflow into the convective margin. For trajectories terminating within the ABL, the flow toward the margin overwhelmingly originates outside of the climatological convection zone in compact regions with relatively little synoptic scatter but some systematic interannual variations. Trajectories terminating in the LFT also reflect widespread inflow conditions, and while the spread in these trajectories tends to be larger than in the ABL, they are sufficiently coherent to permit identification of upstream source regions. However, the LFT source region footprints are often observed to be displaced relative to the ABL. Moreover, as the pdfs of LFT trajectories binned according to climatological precipitation values “sampled” at upstream points indicate, some areas of the margin are characterized by outflow conditions, with air masses arriving from higher mean precipitation values, or a mixture of inflow and outflow conditions.

The expectation based on simple theoretical considerations of an asymmetry in sensitivity of inflow and outflow margins appears to be substantiated, as margin points characterized by outflow or mixed inflow/outflow appear to be relatively insensitive to inflow variability.

Acknowledgments. We thank C.E. Holloway and S.P. Casey for discussion and comments and J.E. Meyerson for graphical assistance. This work was supported by National Oceanic and Atmospheric Administration NA08OAR4310597 and National Science Foundation ATM-0645200.

REFERENCES

- Bretherton, C.S., and A.H. Sobel, 2002: A Simple Model of a Convectively Coupled Walker Circulation Using the Weak Temperature Gradient Approximation. *J. Climate*, **15**, 2907–2920.
- Chaves, R.R., and I.F.A. Cavalcanti, 2001: Atmospheric circulation features associated with rainfall variability over Southern Northeast Brazil. *Mon. Wea. Rev.*, **129**, 2614–2626.
- Chou, C., and J. D. Neelin, 2001, Mechanisms limiting the southward extent of the South American summer monsoon. *Geophys. Res. Lett.*, **28**, no.12, 2433–2436, 2001.
- Chou, C., J.D. Neelin, C.-A. Chen, and J.-Y. Tu, 2009: Evaluating the “rich-get-richer” mechanism in tropical precipitation change under global warming. *J. Climate*,, doi: 10.1175/2008JCLI2471.1.
- Derbyshire, S. H., I. Beau, P. Bechtold, J.-Y. Grandpeix, J.-M. Piriou, J.-L. Redelsperger, and P. M. M. Soares, 2004: Sensitivity of moist convection to environmental humidity. *Quart. J. Roy. Meteor. Soc.*, **130**, 3055–3080.
- Drexler, R.R., and G.D. Hess, 1998: An overview of the Hysplit 4 modelling system for trajectories, dispersion, and deposition, *Austral. Met. Mag.*, **47**, 295–308.
- Frierson, D.M.W., A.J. Majda, and O.M. Pauluis, 2004: Large scale dynamics of precipitation fronts in the tropical atmosphere: A novel relaxation limit, *Comm. Math. Sci.*, **2**, 591–626.
- Giannini, A., J.C.H. Chiang, M.A. Cane, Y. Kushnir, and R. Seager, 2001: The ENSO teleconnection to the tropical Atlantic Ocean: contributions of the remote and local SSTs to rainfall variability in the tropical Americas. *J. Climate*, **14** 4530–4544.
- Hastenrath, S., and L. Greischar, 1993: Circulation mechanisms related to Northeast Brazil rainfall anomalies. *J. Geophys. Res.-Atmos.*, **98**, 5093–5102.
- IPCC, 2007: Climate Change 2007: The Physical Science Basis. Contribution of Working Group

I to the Fourth Assessment Report of the Intergovernmental Panel on Climate Change. Solomon, S., D. Qin, M. Manning (eds.).

Kalnay, E., et al., 1996: The NCEP/NCAR 40-Year Reanalysis Project, *Bull. Amer. Meteor. Soc.*, **77**, 437–471.

Lintner, B.R., and J.D. Neelin, 2007: A prototype for convective margin shifts. *Geophys. Res. Lett.*, **34**, L05812, doi:10.1029/2006GL027305.

Lintner, B.R., and J. D. Neelin, 2008: Eastern margin variability of the South Pacific Convergence Zone. *Geophys. Res. Lett.*, **35**, L16701, doi:10.1029/2008GL034298.

Lintner, B.R., and J. D. Neelin, 2009: Soil moisture impacts on convective margins. *J. Hydrometeor.*, **in press**.

Moscatti, M.C.d.-L., and M.A. Gan, 2007: Rainfall variability in the rainy season of semiarid zone of Northeast Brazil (NEB) and its relation to wind regime, *Int. J. Climatol.*, **27**, 493–512.

Neelin, J.D., and N. Zeng, 2000: A quasi-equilibrium tropical circulation model—formulation. *J. Atmos. Sci.*, **57**, 1741–1766.

Neelin, J.D., C. Chou, and H. Su, 2003: Tropical drought regions in global warming and El Niño teleconnections. *Geophys. Res. Lett.*, **30**, 2275, doi:10.1029/2003GLO018625.

Neelin, J.D., M. Munnich, H. Su, J.E. Meyerson, and C.E. Holloway, 2006: Tropical drying trends in global warming models and observations. *Proc. Nat. Acad. Sci.*, **103**, 6110–6115.

Nobre, P., and J. Shukla, 1996: Variations of sea surface temperature, wind stress, and rainfall over the tropical Atlantic and South America. *J. Climate*, **9**, 2464–2479.

Numaguti, A., R. Oki, K. Nakamura, K. Tsuboki, N. Misawa, T. Asai, and Y.-M. Kodama, 1995: 4-5-day-period variation on low-level dry air observed in the equatorial western Pacific during the TOGA COARE IOP. *J. Meteor. Soc. Japan*, **73**, 267–290.

- Parsons, D.B., K. Yoneyama, J.-L. Reddelsperger, 2000: The evolution of tropical western Pacific atmosphere-ocean system following the arrival of a dry intrusion. *Quart. J. Roy. Meteor. Soc.*, **126**, 517–548.
- Peters, O., and J. D. Neelin, 2006: Critical phenomena in atmospheric precipitation. *Nat. Phys.*, **2**, 393–396, doi:10.1038/nphys314.
- Raymond, D.J., G.B. Raga, C.S. Bretherton, J. Molinari, C. Lopez-Carillo, and Z. Fuchs, 2003: Convective forcing in the intertropical convergence zone of the Eastern Pacific. *J. Atmos. Sci.*, **60**, 2064–2082.
- Redelsperger, J.-L., D. Parsons, and F. Guichard, 2002: Recovery processes and factors limiting cloud-top height following the arrival of a dry intrusion observed during TOGA COARE. *J. Atmos. Sci.*, **59**, 2438–2457.
- Robertson, A.W., and C.R. Mechoso, 2000: Interannual and interdecadal variability of the South Atlantic Convergence Zone. *Mon. Wea. Rev.*, **127**, 2947–2957.
- Sobel, A.H., S.E. Yuter, C.S. Bretherton, and G.N. Kiladis, 2004: Large-scale meteorology and deep convection during TRMM KWAJEX. *Mon. Wea. Rev.*, **132**, 422–444.
- Soden, B.J., and I.M. Held, 2006: Robust responses of the hydrological cycle to global warming. *J. Climate*, **19**, 5686–5699.
- Su, H. and J. D. Neelin, 2005: Dynamical mechanisms for African monsoon changes during the mid-Holocene. *J. Geophys. Res.*, **110**, D19105, doi:10.1029/2005JD005806.
- Takahashi, K., and D. S. Battisti, 2007: Processes controlling the mean tropical Pacific precipitation patterns: The SPCZ and southeast Pacific dry zone. *J. Climate*, **20**, 5696–5706.
- Tompkins, A. M., 2001: Organization of tropical convection in low vertical wind shears: The role of water vapor. *J. Atmos. Sci.*, **58**, 529–545.
- Xie, P., and P.A. Arkin, 1997: Global precipitation: a 17-year monthly analysis based on gauge

observations, satellite estimates, and numerical model outputs. *Bull. Amer. Meteor. Soc.*, **78**, 2359–2558.

Yoneyama, K., and D.B. Parsons, 1999: A proposed mechanism for the intrusion of dry air into the tropical western Pacific. *J. Atmos. Sci.*, **56**, 1524–1546.

Zeng, N., J.-H. Yoon, J.A. Marengo, A. Subramaniam, C.A. Nobre, A. Mariotti, and J.D. Neelin, 2008: Causes and impacts of the 2005 Amazon drought *Environ. Res. Lett.*, **3**, doi: 10.1088/1748-9326/3/1/014002.

Figure Captions

FIGURE 1: (a) JFM climatologies of CMAP precipitation (shaded contours; in mm day^{-1}) and NCEP/NCAR Reanalysis 1000 mb winds (arrows; reference arrow in units of m s^{-1}). Also shown is the 4 mm day^{-1} precipitation contour used as a proxy for the edge of the convection zone. (b) Precipitation along 10°S composited on 1000 mb zonal wind averaged over 45°W - 35°W . The gray line denotes the zonal wind difference ($\times 10$; in m s^{-1}) of anomalous westerly minus easterly conditions. JFM-mean precipitation associated with anomalous westerly (easterly) conditions is in blue (red), with the JFM climatology over all years in black. The purple line represents the precipitation difference normalized by its JFM climatology (in percent).

FIGURE 2: (a) Idealized margin prototype solution for a land-ocean interface. The gray line denotes the total column flux forcing (F_{NET}); the solid blue, green, and red lines are precipitation values for inflow windspeeds of 1, 3, and 5 ms^{-1} , respectively. The black line is the precipitation in the limit of zero windspeed. Dashed lines are vertically-integrated moisture profiles for the 3 nonzero windspeeds. Note that 1 degree is 110 km. Region labels at the top of the figure are referred to in the text. (b) As in (a), but for a smoothly-varying and relatively narrow region with $F_{NET} > 0$.

FIGURE 3: JFM CMAP composite differences conditioned on anomalously high and low precipitation, normalized by the JFM CMAP climatology (shaded contours). Also shown are the 4 mm day^{-1} contours for anomalously high and low precipitation values (green and brown lines, respectively) and composite differences of the (u_{1000}, v_{1000}) .

FIGURE 4: Composite differences of CMAP precipitation conditioned on projection of 1000 mb wind along the mean (a) CMAP precipitation gradient or (b) NCEP/NCAR total precipitable water gradient. Composite differences (in mm day^{-1}) are signed positive for anomalous outflow conditions relative to inflow conditions (arrows). Regions where the JFM precipitation climatology is less than 1 mm day^{-1} have been masked. The green (brown) line denotes the 4 mm day^{-1} precipitation contour for anomalous outflow (inflow) conditions.

FIGURE 5: Ratio of JFM CMAP composite differences in Figure 4a and Figure 3.

FIGURE 6: As in Figure 4, but using 850 mb winds.

FIGURE 7: Comparison JFM climatologies of NCEP/NCAR Reanalysis horizontal winds at 1000 mb (blue) and 850 mb (red). Shaded areas denote gridpoints for which correlations between the inflow-projected components of JFM-mean winds in the ABL and LFT are effectively decoupled, i.e., correlated at less than the 95% level according to a 2-tailed Student t-test.

FIGURE 8: March 5-day back trajectories for selected target points along the convective margin, 2001-2005. Target points are located between mean precipitation values of approximately 3 and 5 mm day⁻¹ at an altitude of 0.5 km. Back trajectories are initialized once-daily at each target point; each color represents a different year of 31 March trajectories: 2001 (red), 2002 (yellow), 2003 (green), 2004 (blue), and 2005 (purple). Filled contours denote the March climatology of CMAP precipitation (units of mm day⁻¹).

FIGURE 9: As in Figure 8, but for target points at 2.0 km.

FIGURE 10: Probability distribution functions of CMAP precipitation values sampled along HYSPLIT back trajectories for the nine 2.0 km target points in Figure 9. The results shown here are for March for all years spanning 1979-2006. PDFs are shown for time intervals of 48, 72, and 96 hours upstream of the target points. The black (gray) data use the climatological (yearly) March precipitation values. The vertical dashed lines denote the climatological March value of precipitation at each target point.

FIGURE 11: 5-Day March backward (solid) and forward (dashed) trajectories and composited on CMAP March precipitation values at 40°W, 11.25°S (denoted by X). Positive (negative) phase trajectories are shown in blue (red). The backward trajectories are initialized at 40°W, 11.25°S, and 2.0 km, while the forward trajectories are initialized at 30°W, 10°S, and 1.6 km. Numerical labels denote 24 hour increments along the trajectories.

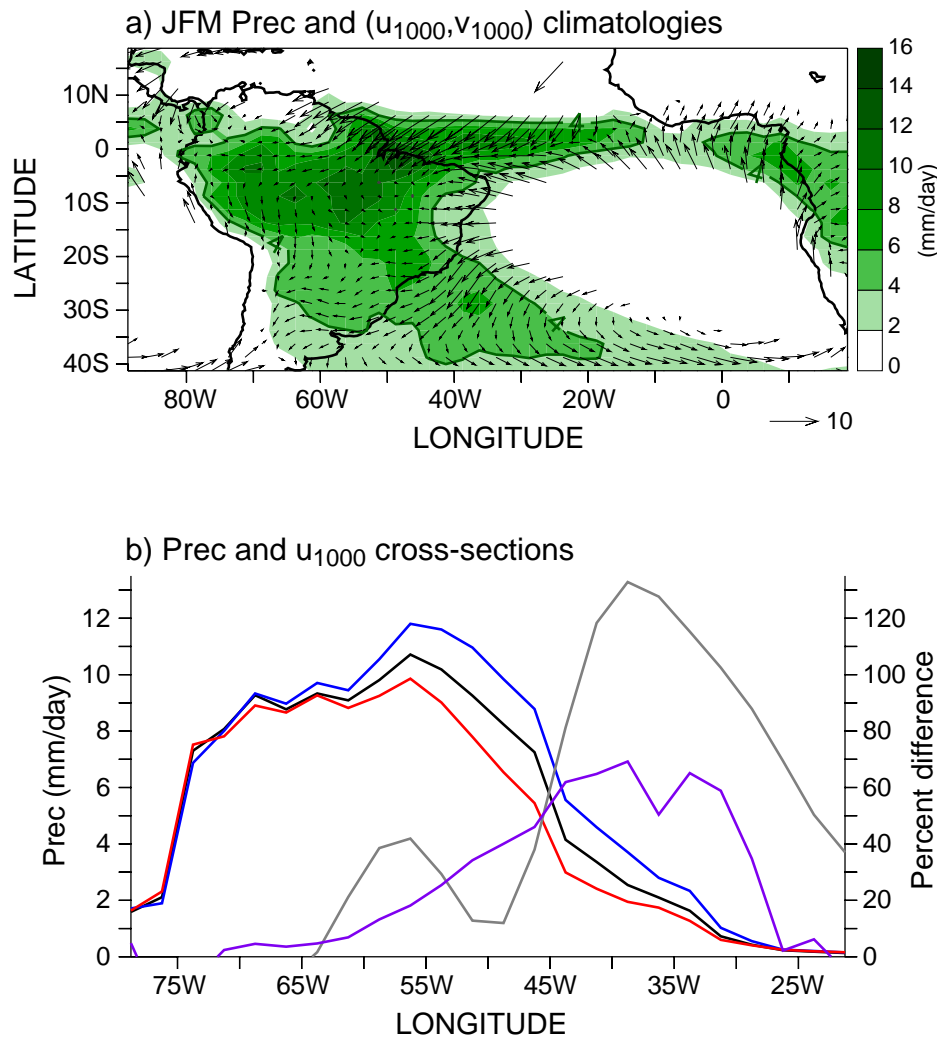


FIGURE 1: (a) JFM climatologies of CMAP precipitation (shaded contours; in mm day^{-1}) and NCEP/NCAR Reanalysis 1000 mb winds (arrows; reference arrow in units of m s^{-1}). Also shown is the 4 mm day^{-1} precipitation contour used as a proxy for the edge of the convection zone. (b) Precipitation along 10°S composited on 1000 mb zonal wind averaged over 45°W - 35°W . The gray line denotes the zonal wind difference ($\times 10$; in m s^{-1}) of anomalous westerly minus easterly conditions. JFM-mean precipitation associated with anomalous westerly (easterly) conditions is in blue (red), with the JFM climatology over all years in black. The purple line represents the precipitation difference normalized by its JFM climatology (in percent).

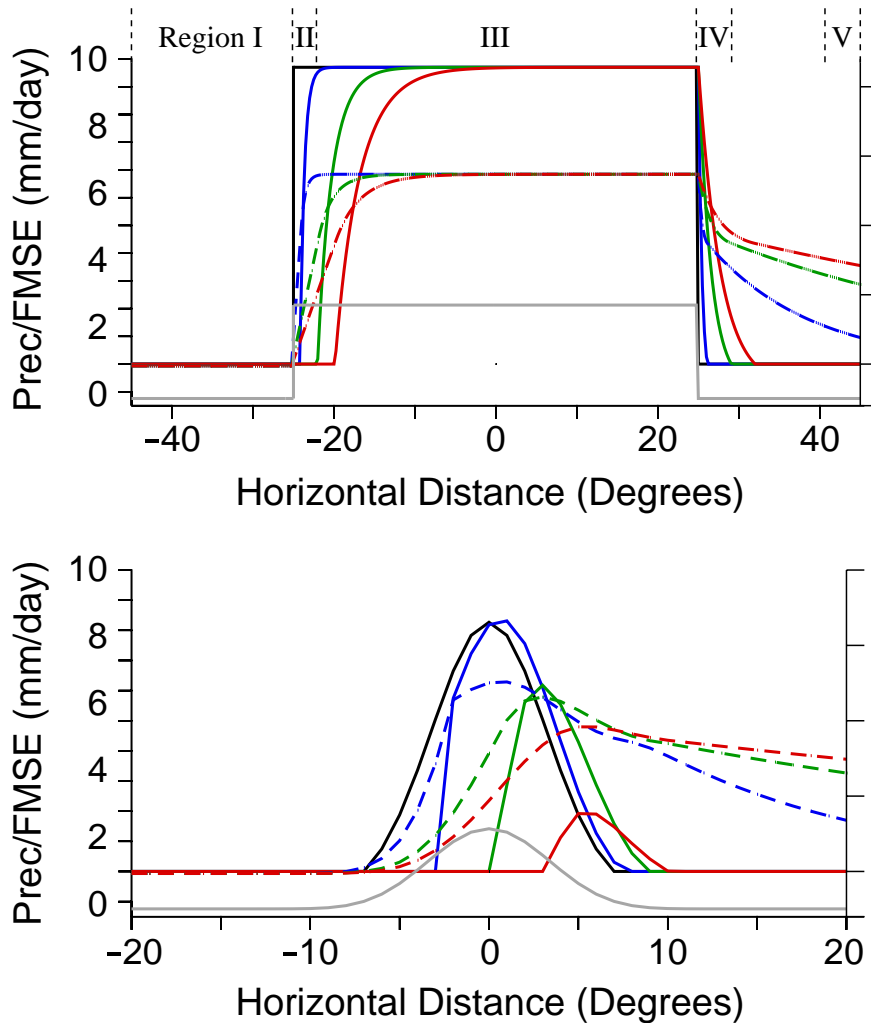


FIGURE 2: (a) Idealized margin prototype solution for a land-ocean interface. The gray line denotes the total column flux forcing (F_{NET}); the solid blue, green, and red lines are precipitation values for inflow windspeeds of 1, 3, and 5 ms^{-1} , respectively. The black line is the precipitation in the limit of zero windspeed. Dashed lines are vertically-integrated moisture profiles for the 3 nonzero windspeeds. Note that 1 degree is 110 km. Region labels at the top of the figure are referred to in the text. (b) As in (a), but for a smoothly-varying and relatively narrow region with $F_{NET} > 0$.

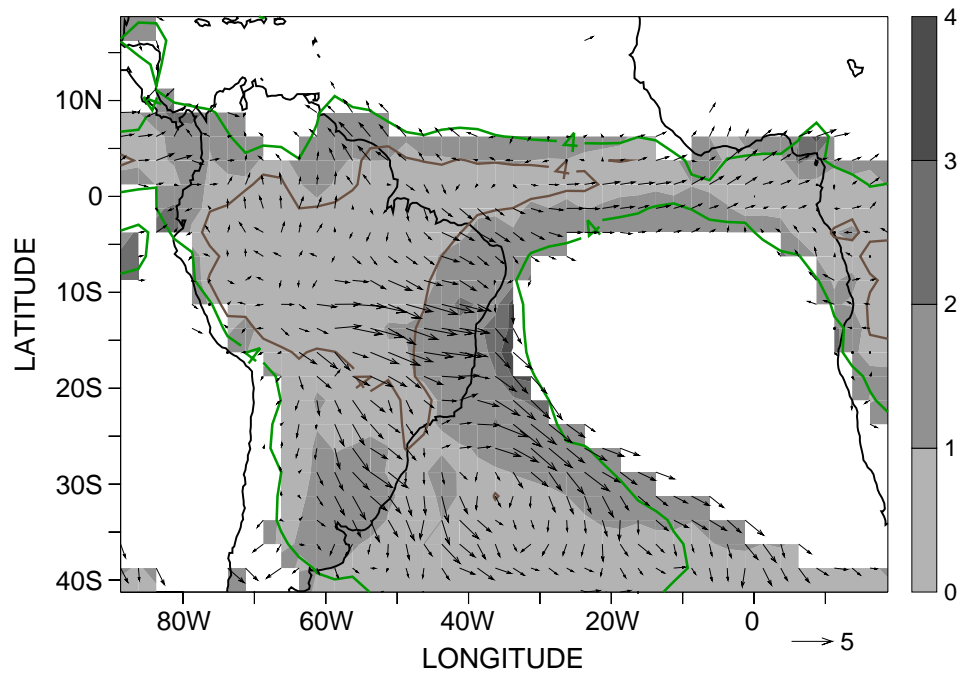


FIGURE 3: JFM CMAP composite differences conditioned on anomalously high and low precipitation, normalized by the JFM CMAP climatology (shaded contours). Also shown are the 4 mm day^{-1} contours for anomalously high and low precipitation values (green and brown lines, respectively) and composite differences of the (u_{1000}, v_{1000}) .

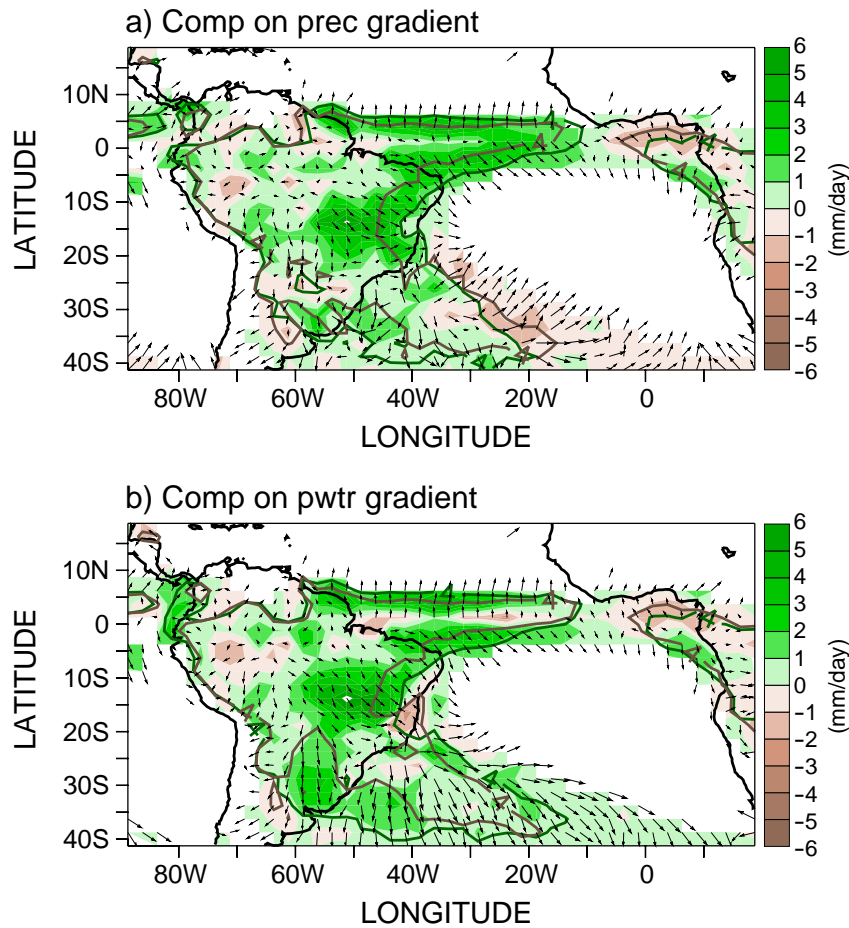


FIGURE 4: Composite differences of CMAP precipitation conditioned on projection of 1000 mb wind along the mean (a) CMAP precipitation gradient or (b) NCEP/NCAR total precipitable water gradient. Composite differences (in mm day^{-1}) are signed positive for anomalous outflow conditions relative to inflow conditions (arrows). Regions where the JFM precipitation climatology is less than 1 mm day^{-1} have been masked. The green (brown) line denotes the 4 mm day^{-1} precipitation contour for anomalous outflow (inflow) conditions.

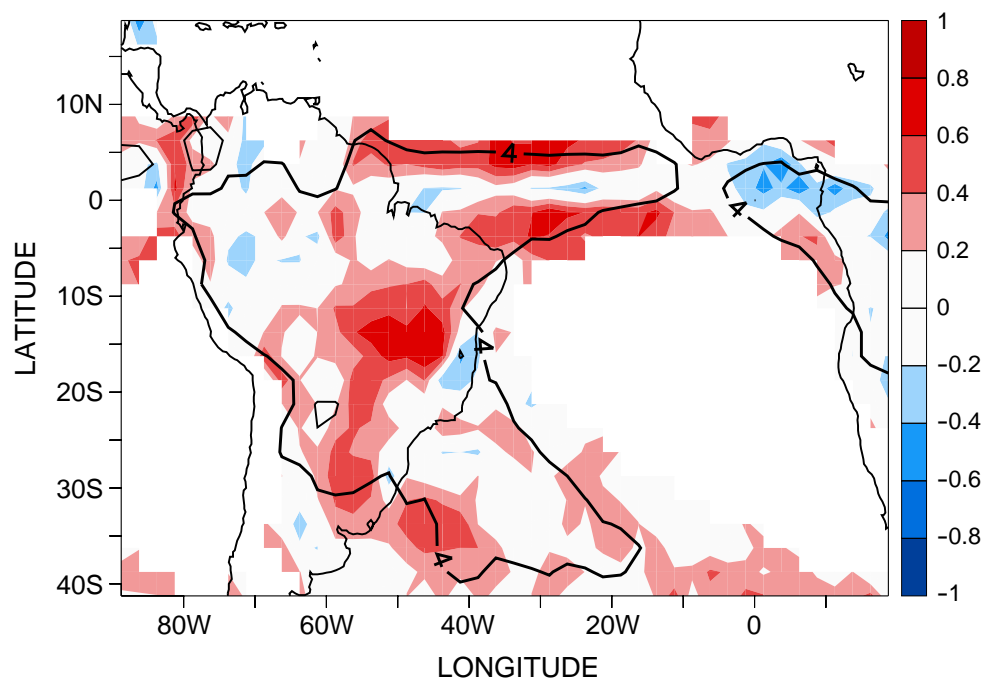


FIGURE 5: Ratio of JFM CMAP composite differences in Figure 4a and Figure 3.

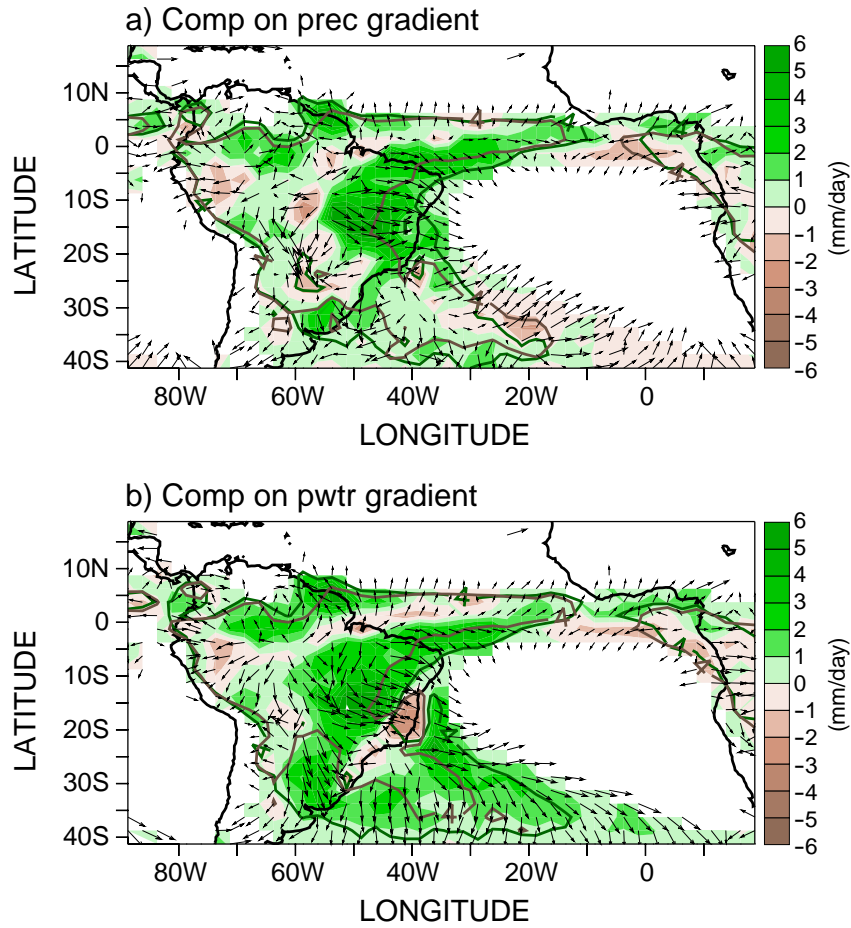


FIGURE 6: As in Figure 4, but using 850 mb winds.

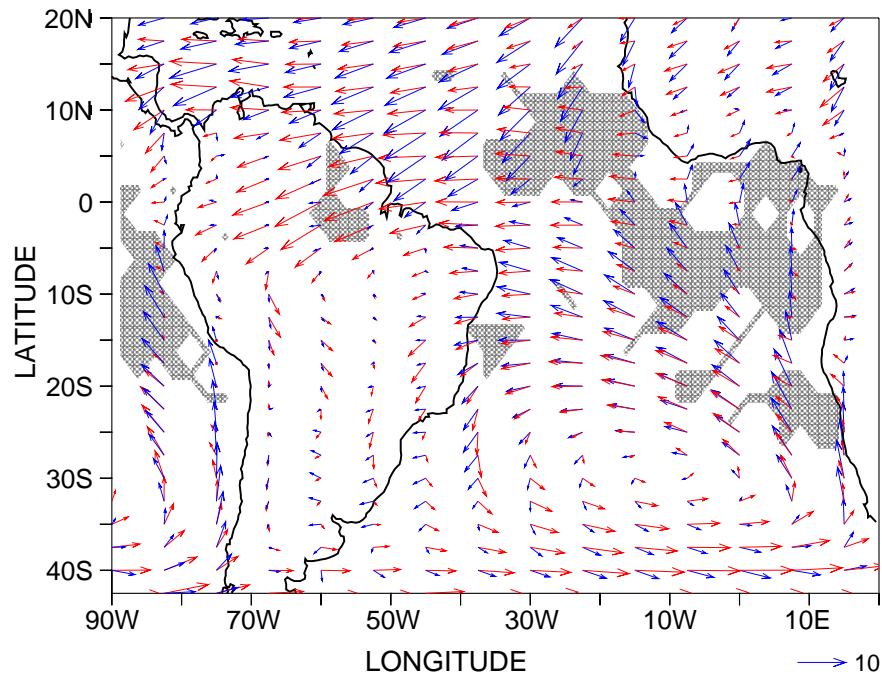


FIGURE 7: Comparison JFM climatologies of NCEP/NCAR Reanalysis horizontal winds at 1000 mb (blue) and 850 mb (red). Shaded areas denote gridpoints for which correlations between the inflow-projected components of JFM-mean winds in the ABL and LFT are effectively decoupled, i.e., correlated at less than the 95% level according to a 2-tailed Student t-test.

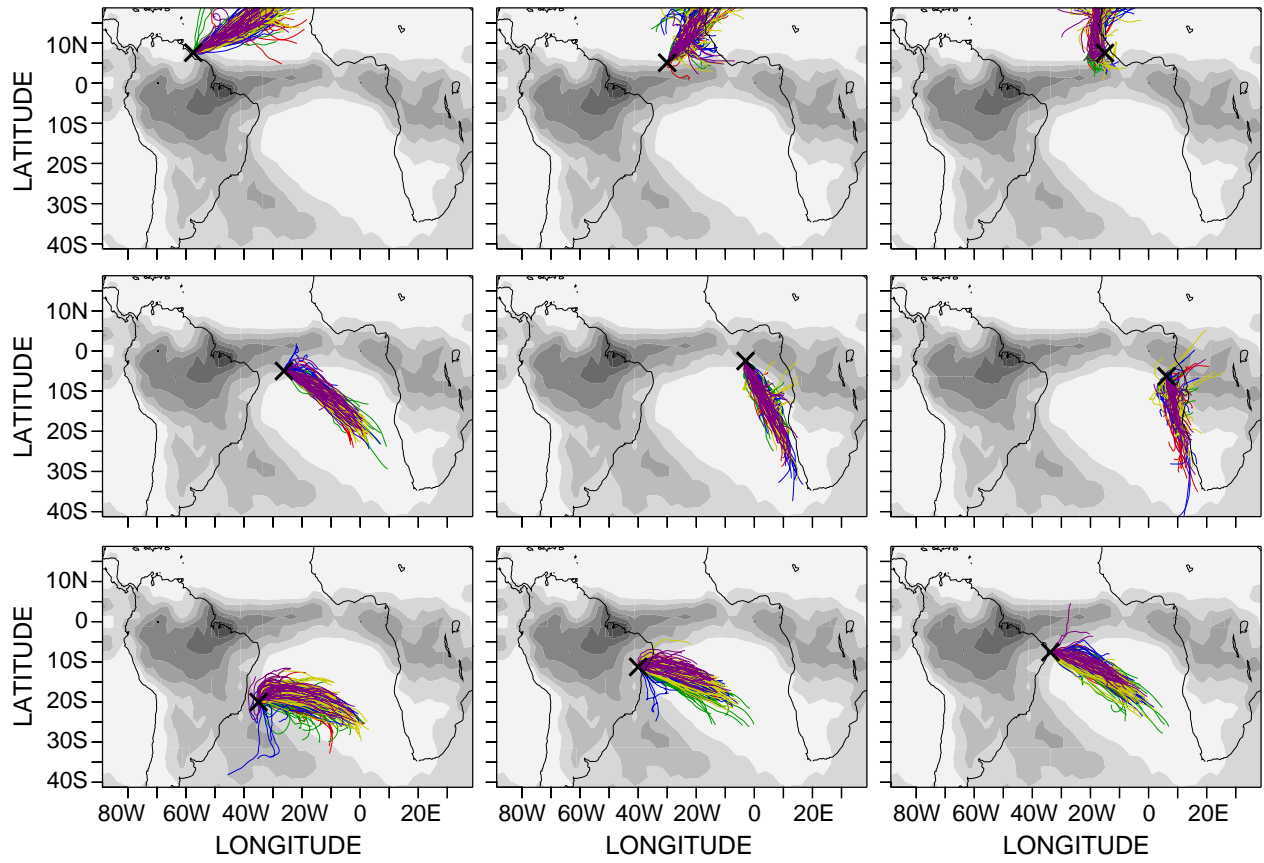


FIGURE 8: March 5-day back trajectories for selected target points along the convective margin, 2001-2005. Target points are located between mean precipitation values of approximately 3 and 5 mm day⁻¹ at an altitude of 0.5 km. Back trajectories are initialized once-daily at each target point; each color represents a different year of 31 March trajectories: 2001 (red), 2002 (yellow), 2003 (green), 2004 (blue), and 2005 (purple). Filled contours denote the March climatology of CMAP precipitation (units of mm day⁻¹).

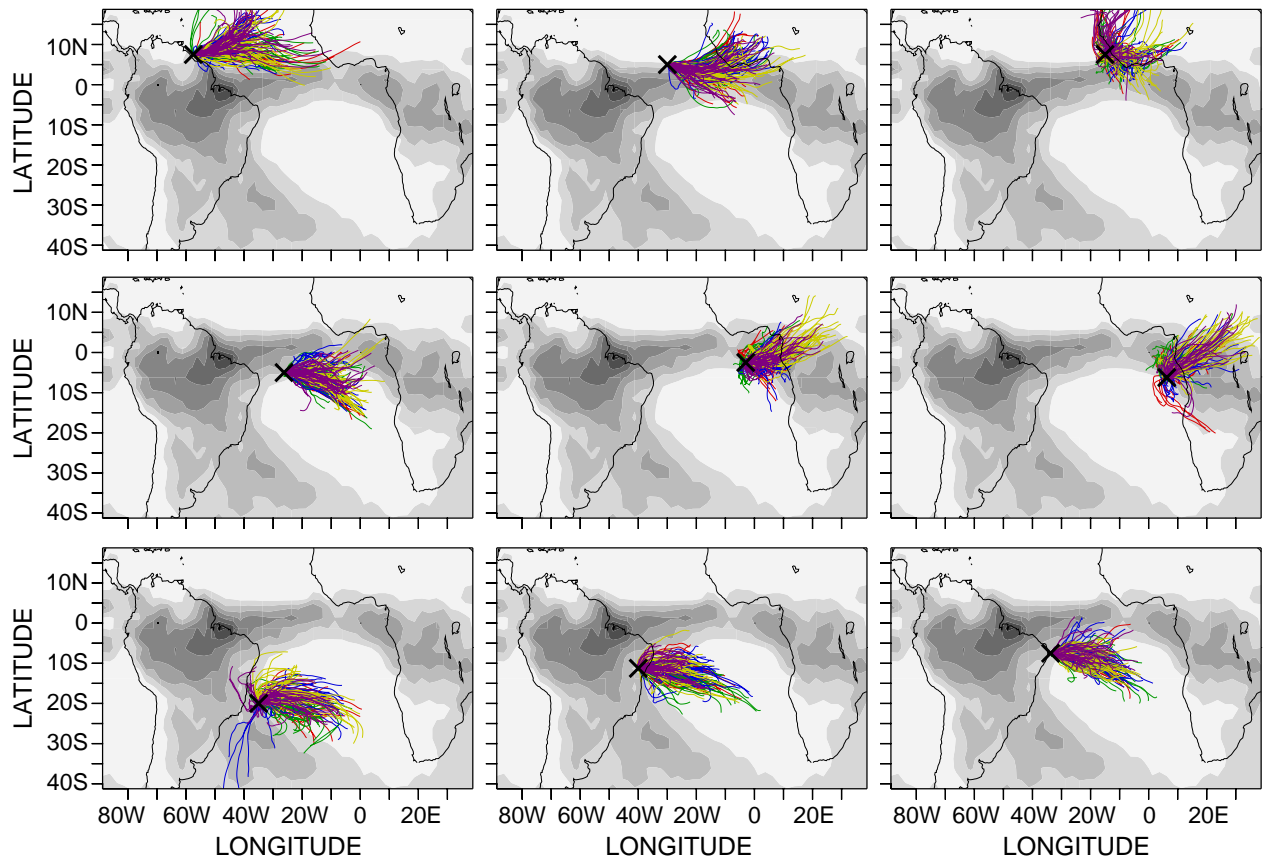


FIGURE 9: As in Figure 8, but for target points at 2.0 km.

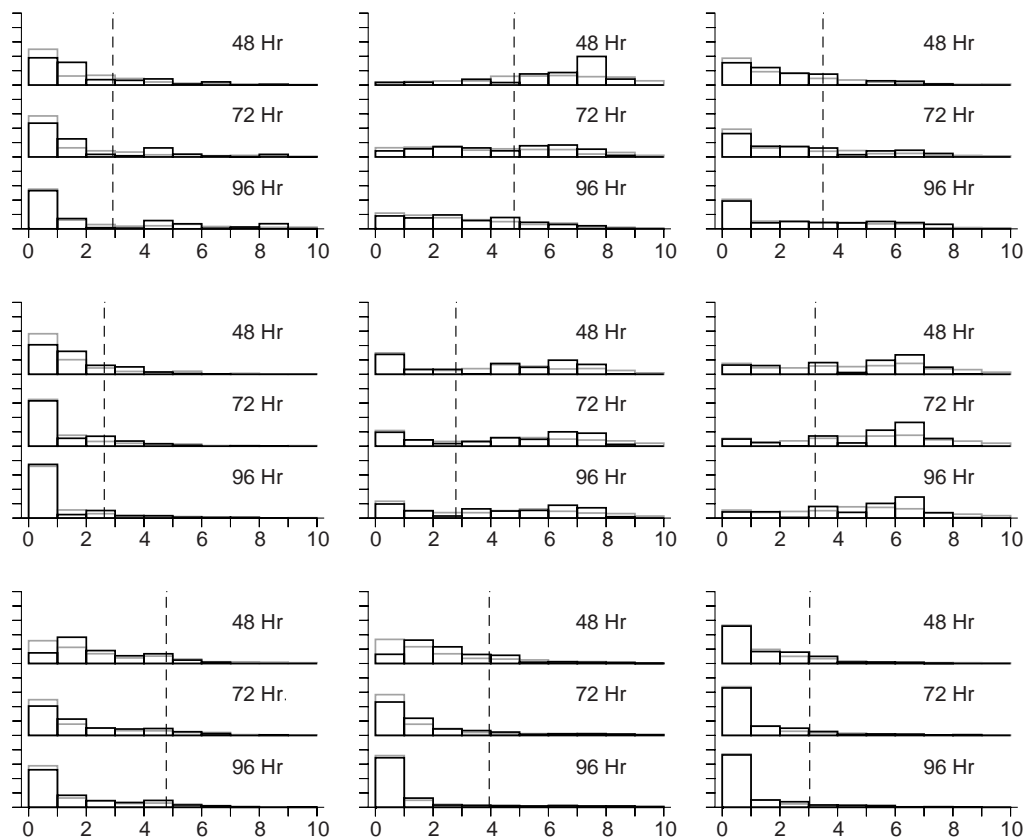


FIGURE 10: Probability distribution functions of CMAP precipitation values sampled along HYSPLIT back trajectories for the nine 2.0 km target points in Figure 9. The results shown here are for March for all years spanning 1979-2006. PDFs are shown for time intervals of 48, 72, and 96 hours upstream of the target points. The black (gray) data use the climatological (yearly) March precipitation values. The vertical dashed lines denote the climatological March value of precipitation at each target point.

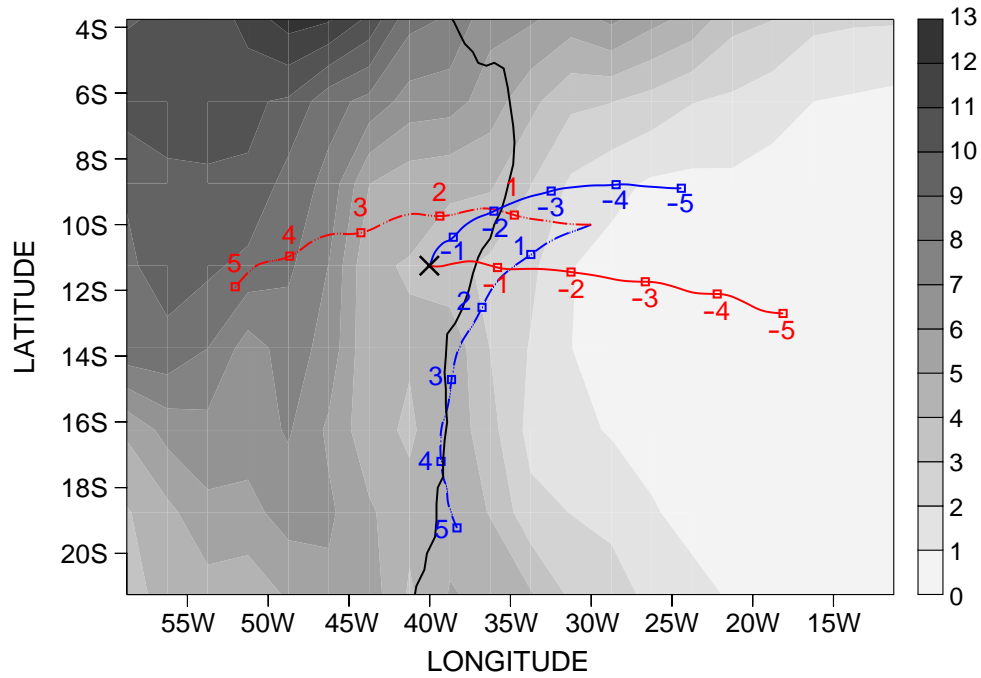


FIGURE 11: 5-Day March backward (solid) and forward (dashed) trajectories and composited on CMAP March precipitation values at 40°W , 11.25°S (denoted by X). Positive (negative) phase trajectories are shown in blue (red). The backward trajectories are initialized at 40°W , 11.25°S , and 2.0 km, while the forward trajectories are initialized at 30°W , 10°S , and 1.6 km. Numerical labels denote 24 hour increments along the trajectories.